nature astronomy

LETTERS

https://doi.org/10.1038/s41550-019-0958-x

Cascading parallel fractures on Enceladus

Douglas J. Hemingway[1,2*], Maxwell L. Rudolph[3] and Michael Manga[2]

Active eruptions from the south polar region of Saturn's ~500-km-diameter moon Enceladus are concentrated along a series of lineaments known as the 'tiger stripes'[1,2], thought to be partially open fissures that connect to the liquid water ocean beneath the ice shell[3,4]. To date, no study simultaneously explains why the tiger stripes should be located only at the south pole, why there are multiple approximately parallel and regularly spaced fractures, what accounts for their spacing of about 35 km, and why similarly active fissures have not been observed on other icy bodies. Here we propose that secular cooling, which leads to a thickening of the ice shell and building of global tensile stresses[5,6], causes the first fracture to form at one of the poles, where the ice shell is thinnest owing to tidal heating[7]. The tensile stresses are thereby relieved, preventing a similar failure at the opposite pole. The steadily erupting water ice loads the flanks of the open fissure, causing bending in the surrounding elastic plate and further tensile failure in bands parallel to the first fracture—a process that may be unique to Enceladus, where the gravity is too weak for compressive stresses to prevent fracture propagation through the thin ice shell. The sequence of fissures then cascades outwards until the loading becomes too weak or the background shell thickness becomes too great to permit through-going fractures.

To explain the polar location of the tiger stripes, we connected the shell structure predictions from a tidal heating model[7] with a thermal evolution scenario and associated tensile-failure model[5,6]. To explain the regular spacing of the tiger stripes, we then modelled the elastic bending stresses resulting from loading at the edge of the first fracture and the consequent initiation of parallel fractures.

Given that the erupted ice grains appear to be sampling the internal liquid-water ocean[8–10], the tiger stripes may be taken as open fissures that fully penetrate the ice shell[11]. Accordingly, although the south polar region bears evidence of a complex geologic history[12–15], most studies presume an extensional origin for the tiger stripes. Whereas Yin et al.[14,15] suggest a strike-slip origin for the tiger stripes, attributing their regular spacing to a stress shadowing effect, we regard an extensional origin as more likely because it can create open conduits directly to the underlying liquid ocean, allowing the eruptions to be initiated and sustained by controlled boiling[11,16].

Over time, changes in the semi-major axis and eccentricity of the orbit of Enceladus will alter the efficacy of tidal heating—the primary source of internal heat production for Enceladus[17]. Even if Enceladus is close to a steady-state configuration, in which viscous relaxation at the base of the ice shell is counterbalanced by ongoing freezing and melting[18,19], any period of gradual secular cooling will result in some net freezing of the ocean. As long as there exists a layer within the ice shell that is free of active faults and capable of accumulating tensile stresses, the volume increase associated with the phase change from water to ice will result in ocean pressurization[5] (Methods). As freezing progresses, tangential stresses build until the tensile failure limit is exceeded somewhere in the ice shell (Fig. 1 and Supplementary Fig. 1). Since tidal heating should cause the shell to be thinnest at the poles[7,20], tangential stresses are maximized at the poles such that the initial failure should occur at one of the poles, with either being equally likely. In contrast to previous work[21–23], this mechanism thus accounts for the polar concentration of the eruptive activity without requiring true polar wander. Although periods of secular heating and net melting of the ice shell have also probably occurred, especially if Enceladus began cold, this would have generated compressive stresses and thrust faulting. Because such faults do not readily produce open fissures, however, we do not favour compressive failure as the mechanism primarily responsible for the formation of the tiger stripes.

Whereas the cold upper part of the ice shell behaves elastically, the warmer ice toward the base of the shell behaves viscously on long timescales (Methods). Provided that the ductile portion of the ice shell is not too thick, however, the fracture can penetrate the entire ice shell, establishing an open pathway directly to the underlying ocean[6] (Supplementary Fig. 2). Crucially, once the first fissure forms, the ocean overpressure is relieved, removing the mechanism for generating large, global tangential stresses. That is, it is no longer possible for a similar fracture to develop at the opposite pole, or anywhere else. In contrast with previous models involving diapirs or impact events[21–23], our model thus accounts for the concentration of activity at a single pole by virtue of the fact that the critical pressure- and stress-relieving failure can occur only once.

We therefore suggest that Baghdad Sulcus, which cuts directly through the geographic south pole, was the first fracture to form and that the remaining fractures formed through a distinct, though related, process (see below). Baghdad's orientation of ~30° from the tidal axis approximately maximizes normal tensile stresses arising due to diurnal tidal deformation[24]. Although these tidal stresses are weaker (~14–85 kPa), when combined with the isotropic background tensile stress field resulting from ocean pressurization, the total could be sufficient to cause failure. This may explain the orientation of the tiger stripes, provided that the ice shell has not experienced non-synchronous rotation since their formation.

Once the first open fissure has formed, liquid water rises to the level of neutral buoyancy (the lower 90% becomes filled with water) and begins to boil off at the top, where it is exposed to the vacuum. Whereas ocean overpressure was important for forming the first fracture, it is relieved once that fissure is open, and does not therefore contribute to driving the eruptions themselves (Methods), which are instead driven by controlled boiling[16]. Turbulent dissipation associated with tidally driven cyclic flushing and refilling of the liquid-filled fissure can prevent it from freezing shut[4]. Provided these (or similar) mechanisms can maintain the stability of such

[1]Department of Terrestrial Magnetism, Carnegie Institution for Science, Washington, DC, USA. [2]Department of Earth & Planetary Science, University of California Berkeley, Berkeley, CA, USA. [3]Department of Earth & Planetary Sciences, University of California Davis, Davis, CA, USA. *e-mail: dhemingway@carnegiescience.edu

ocean-to-surface pathways, the eruptions may persist for extended periods. Some 91% of the erupted solids fall ballistically back to the surface of Enceladus[25], accumulating preferentially on the flanks of the open fissures[26], possibly explaining the origin of the ridges observed along the tiger stripes[27].

If the cold upper part of the ice shell behaves elastically, both the material accumulated on the flanks of the open fissure and the loss of buoyancy associated with any localized ice-shell thinning act like downward forces applied near the edge of the broken elastic plate, causing bending stresses to develop in the surrounding ice shell[28,29] (Supplementary Fig. 3). Given a load acting at the edge of the broken plate, it can be shown that the maximum bending stresses occur at a distance from the first fracture

$$x_m = \alpha\frac{\pi}{4} \quad (1)$$

where α is the characteristic length scale for elastic flexure, given by

$$\alpha^4 = \frac{ET_e^3}{3\rho_w g(1-\nu^2)} \quad (2)$$

where E and ν are the Young's modulus and Poisson's ratio for the icy shell, g is the acceleration due to gravity, ρ_w is the density of the ocean, and T_e is the effective elastic-layer thickness. If the typical tiger-stripe spacing of ~35 km is governed by the position where maximum bending stresses occur, then, assuming $E = 9$ GPa, $\nu = 0.25$ and $\rho_w = 1{,}020\,\mathrm{kg\,m^{-3}}$, and with $g = 0.113\,\mathrm{m\,s^{-2}}$, we obtain $T_e \approx 5.2$ km (Supplementary Fig. 4). Given the expected temperature structure of the ice shell, this corresponds to a total local shell thickness of roughly 8–9 km (Methods), consistent with the south-polar shell thickness inferred from gravity, topography and librations[7]. Approximating the load as a line load, V_0, acting at the edge of the broken plate, it can be shown (Methods) that the resulting bending causes maximum tensile stresses at x_m to reach

$$\sigma_{max} = V_0\frac{6}{T_e^2}\alpha\, e^{-\pi/4}\sin\frac{\pi}{4} \quad (3)$$

Bending stresses can thus initiate secondary fractures in bands parallel to the first fracture once the load acting at the edge of the plate is sufficient to cause σ_{max} to exceed the tensile failure limit for ice, σ_{crit}. Although localized ice-shell thinning could, in principle, contribute to the bending of the plate, the process may be self-limiting because the melting ice is opposed by viscous closure and the freezing that results from reduced local turbulent dissipation, making this effect too small to produce the necessary loading[4] (Methods and Supplementary Fig. 5). A more effective source of edge loading may be the accumulation of erupted material onto the ridges flanking the open fissure. The eruption rate and the fraction of erupted material falling back onto the ridges determines the time required before the bending stresses cause tensile failure and the initiation of a secondary fracture (Supplementary Fig. 6). If, for example, the eruption rate of the solids from a single fissure is $20\,\mathrm{kg\,s^{-1}}$ and if 91% of this material goes into the formation of the flanking ridges, then, taking the fissure length to be 100 km, the loading on each ridge reaches the critical value after ~1 Myr assuming $\sigma_{crit} = 1$ MPa (Methods).

As the secondary fracture begins to propagate, the broken portion of the elastic plate can no longer contribute to supporting the bending moment and the effective elastic thickness is reduced. Assuming that the load is not changing on the timescale of fracture propagation, the stress profile in the elastic plate becomes increasingly steep,

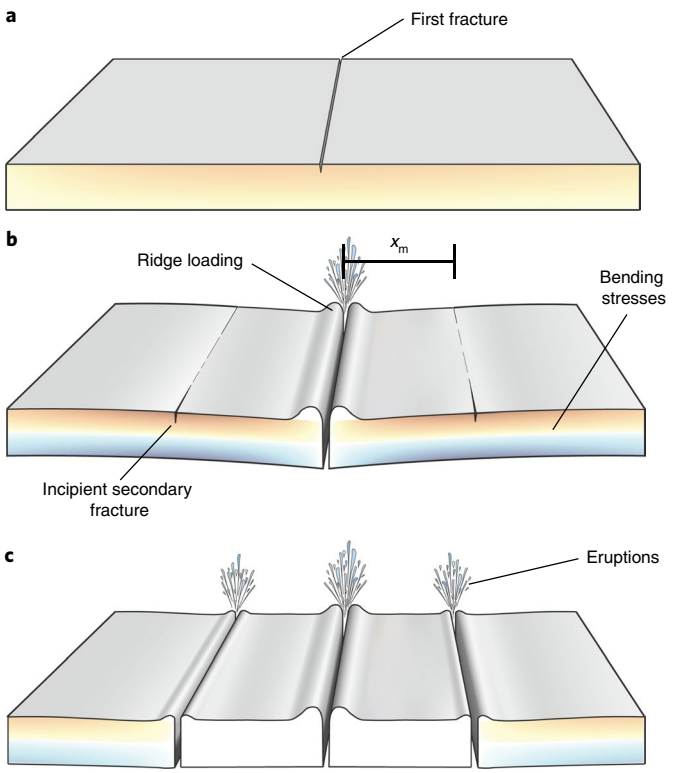

Fig. 1 | Proposed sequence for tiger-stripe formation. a, The global tensile stress field (orange shading) arising from secular cooling and the consequent ocean pressurization leads to tensile failure at one of the poles, where the ice shell is thinnest. **b**, Following the first fracture's formation, the erupting solids then accumulate preferentially in ridges flanking the open fissure, loading the edge of the broken ice shell and producing bending stresses in the surrounding elastic plate (orange and blue shades indicate tensile and compressive stresses, respectively, in the elastic layer; the ductile layer is not shown). The bending stresses eventually become large enough to initiate a set of secondary fractures parallel to the first and at a distance, x_m, determined by the ice shell's elastic properties, according to equation (1). **c**, Once open, the secondary fractures then develop in a fashion similar to the first, resulting in a cascading sequence of parallel fissures.

with the crack-tip stress being always tensile and increasing steadily as the fracture propagates. This effect is countered by the compressive stresses from overburden pressure, which increase with depth (Supplementary Fig. 7). For Enceladus, however, gravity is so weak that such compressive stresses are not important and the crack-tip stresses are always increasing as the crack propagates, meaning that the crack should penetrate rapidly through the entire elastic layer. For larger icy-ocean worlds, the gravity is generally too strong to allow the crack-tip stress to build in this way, potentially explaining why similarly active fissures are not observed on other bodies (Fig. 2 and Methods).

Although roughly the lower 40% of the ice shell is ductile on long timescales (Methods), it may behave elastically on the timescale of fracture propagation, such that the secondary fracture can penetrate all the way through to the ocean—though future work is required to model the full viscoelastic nature of this problem. Once a through-going fracture is established in this way, it evolves in a fashion similar to the first fracture, allowing the sequence to cascade outward from the original fracture in symmetric pairs (Fig. 1): after Baghdad, Cairo and Damascus, then Alexandria and the feature informally named 'E' by Yin and Pappalardo[14]. Although the driving processes and geometries differ, loading-induced stresses

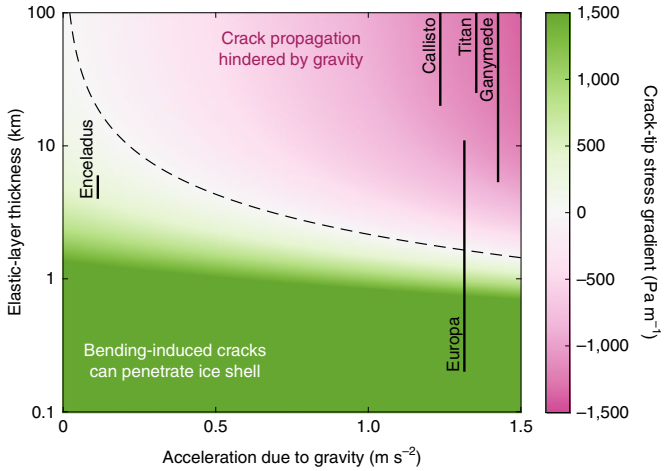

Fig. 2 | Crack-tip stress gradient. Change in tip stress as the crack propagates, as a function of surface gravity and effective elastic-layer thickness, given by equation (31). Positive values (green) correspond to conditions that permit the crack-tip stress to become increasingly tensile as the crack propagates. Negative values (magenta) correspond to conditions in which the compressive stresses due to overburden pressure build too rapidly to permit crack propagation immediately following the initial bending-stress-induced failure (Supplementary Fig. 7). The dashed black contour represents the transition between the two regimes. The vertical black lines represent the estimated ranges of elastic-layer thicknesses for icy-ocean worlds.

have similarly been invoked to explain the spacing of hotspot volcanoes on Earth[30,31].

There are several ways in which the cascade may be arrested. If the eruption rate becomes too slow, bending stresses may not reach the critical value on a timescale for which the ice behaves elastically. If the eruption rate through each fissure decreases as new fissures are formed, those forming later may not be loaded quickly enough for the resulting bending stresses to generate additional fractures. Fractures forming farther from the pole, where the background ice-shell thickness is greater, may also have a more difficult time propagating through the thicker ductile part of the ice shell.

Finally, although our model may be able to account for the initial formation of the tiger stripes, other processes, such as tidal and gravitational stresses, may continue to rework the fissures, forming strike-slip features[14,15] or the funiscular plains[13], for example. We emphasize that, in spite of the youthful appearance of the south-polar terrain, and our conclusion that the total south-polar shell thickness at the time of tiger-stripe formation is close to the present-day value of ~9 km, the continuing eruptive activity, along with ongoing tidal reworking, could keep the surface young even if the tiger-stripe fractures did not form recently. Likewise, our results are not incompatible with stratigraphically older features having formed through similar or distinct processes that may have operated prior to the formation of the currently active fissures as part of the south polar region's evidently complex geologic history[12–15].

Methods

Temperature structure. The total ice-shell thickness (d) and the effective elastic thickness (T_e) are related by the temperature structure of the ice shell. For a conductive ice shell, accounting for the temperature-dependent thermal conductivity, which goes as T^{-1}, the temperature structure is given by[32]

$$T(z) = T_s\left(\frac{T_b}{T_s}\right)^{z/d} \tag{4}$$

where z is the depth below the surface and where T_s and T_b are the surface and basal temperatures, respectively. On long timescales, the warmer parts of the ice shell behave viscously while the coldest parts of the ice remain elastic[33]. If we assume that the ductile layer corresponds to the ice that is warmer than 160–180 K, then from (4), and assuming $T_s = 75$ K and $T_b = 273$ K, we obtain $T_e/d \approx 0.59$–0.68.

Tensile-stress accumulation due to secular cooling. Beginning with equations (2)–(5) by Manga and Wang[5], we obtain a set of analytical expressions that capture the effects of ocean overpressure and ice-shell tensile-stress accumulation resulting from secular cooling and the corresponding ice-shell thickening. Following their[5] notation, we assume an ice shell of outer radius R and inner radius r_i above a global liquid-water ocean over a rocky core of radius r_c. Taking the ice and water densities to be ρ_i and ρ_w, respectively, it can be shown that the excess pressure in the ocean resulting from freezing a thickness of water h is given by

$$P_{ex} = \frac{h\left(1-\frac{\rho_i}{\rho_w}\right)}{\frac{\beta(r_i^3-r_c^3)}{3r_i^2}+\frac{\xi}{E}\left(1+2\nu\frac{1+\frac{1}{2}\left(\frac{R}{\xi}\right)^3}{\left(\frac{R}{\xi}\right)^3-1}\right)} \tag{5}$$

where ξ is the radius corresponding to the base of the elastic layer ($\xi = R - T_e$) and $\beta = 4\times10^{-10}$ Pa^{-1} is the compressibility of water. This excess ocean pressure drives tangential stresses in the ice shell that, when evaluated at $r = R$, are given by

$$\sigma_t = \frac{3}{2}\frac{P_{ex}}{\left(\frac{R}{\xi}\right)^3-1} \tag{6}$$

Supplementary Fig. 1 shows that, starting with an unbroken ice shell that is capable of supporting global-scale tangential stresses, a few hundred metres of ocean freezing is sufficient to cause tensile failure in the ice shell.

Manga and Wang[5] assumed a uniform ice shell such that there was no preferred location for the tensile failure. For the purposes of the above calculation, we have made the same assumption. However, whereas a non-uniform ice-shell thickness should not meaningfully affect the above result[34], it does affect the preferred location for the tensile failure, as stresses will concentrate in the thinnest parts of the shell. Even before the initiation of eruptive activity, the ice shell is expected to have been thinnest at the poles due to the non-uniform distribution of tidal heating[7]. Hence, tangential stresses resulting from secular cooling should have been concentrated at both poles, with tensile failure being equally likely to occur at either pole. Although they are an order of magnitude smaller, tidal stresses and stresses associated with topographic anomalies will also affect the stress field and may contribute to determining the precise location and orientation of the first failure.

Propagation of initial fracture. Once initiated at the surface (Fig. 1a), tensile cracks will propagate downward on a timescale that is rapid compared with the Maxwell time. We develop a model based on linear elastic fracture mechanics to calculate the maximum depth of penetration of fractures. As the subsurface ocean is pressurized, tensile stresses are generated globally in the elastic layer (we assume that stresses do not accumulate in the lower, warmer part of the ice), and if these stresses exceed the tensile strength of ice, a fracture will initiate at the surface and propagate downward. The model from the previous section always predicts maximum tensile stresses at the surface, rather than at intermediate depths within the ice shell. If the tip of the fracture extends below the stressed elastic layer, the upper region of the crack is under tension but the tip of the crack is under compression due to overburden pressure. We model the downward propagation of the fracture under the assumption that the entire ice shell behaves as a linear elastic solid on the timescale of crack propagation but that only the elastic layer supports tensile stresses that encourage fracture penetration. We use a boundary-element code based on the displacement discontinuity method[35], extended to include a crack-tip element[6] to more accurately resolve the stress field near the crack tip. In each calculation, we initiate a short crack near the surface, extending to one-half the depth (d_c) where lithostatic compression balances the applied tensile stress (σ_t)

$$\int_0^{T_e}\sigma_t\,dz = \int_0^{d_c}\rho_i g z\,dz \tag{7}$$

where z is depth from the surface. We note that this formula is similar to the maximum depth of fracture penetration from Qin et al.[36], except that we account for the presence of a viscous ice layer. We solve for d_c, obtaining

$$d_c = \sqrt{\frac{2T_e\sigma_t}{\rho_i g}} \tag{8}$$

We calculate the mode-I stress intensity factor K_I, describing the magnitude of stresses near the crack tip. Next, we incrementally extend the crack length, computing a new solution for displacements and K_I for each successive crack

length. The crack is arrested if $K_I < 0$, which is equivalent to assuming zero fracture toughness. Our numerical and analytical results are in good agreement with one another (Supplementary Fig. 2) and are consistent with earlier work[6].

Bending stresses. The load acting at the edge of the broken plate causes bending stresses to develop in the elastic part of the ice shell[28,29,37]. We assume that the ice shell is completely broken and that there are no remaining horizontal loads—we neglect membrane stresses since they cannot be transmitted across the open fissure. Approximating the problem in a Cartesian geometry, and assuming cylindrical bending, the bending moment at any given point is given by

$$M(x) = D\frac{\mathrm{d}^2 w}{\mathrm{d}x^2} \tag{9}$$

where w is the deflection, x is the horizontal distance increasing away from the fracture and D is the flexural rigidity, given by

$$D = \frac{ET_e^3}{12(1-\nu^2)} \tag{10}$$

We assume that the flexural rigidity does not vary with x. The load is related to the deflection by

$$D\frac{\mathrm{d}^4 w}{\mathrm{d}x^4} + \rho_w g w = q(x) \tag{11}$$

(we assume only vacuum exists above the ice shell).

For a line load acting at the edge of the broken plate, it can be shown[28] that the deflection is given by

$$w = \frac{V_0 \alpha^3}{2D} \mathrm{e}^{-x/\alpha} \cos\frac{x}{\alpha} \tag{12}$$

where V_0 has units of N m^{-1} and where α is given by

$$\alpha^4 = \frac{4D}{\rho_w g} \tag{13}$$

It can be shown that the bending moment per unit length along the fracture (units of N) is then given by

$$M(x) = V_0 \alpha\ \mathrm{e}^{-x/\alpha} \sin\frac{x}{\alpha} \tag{14}$$

The maximum bending moment occurs where $\mathrm{d}M/\mathrm{d}x = 0$, at

$$x_m = \alpha\frac{\pi}{4} \tag{15}$$

The fibre stresses within the plate can be written

$$\sigma_{xx}(x,z) = \frac{12M(x)}{T_e^3}\left(\frac{T_e}{2} - z\right) \tag{16}$$

where z is the vertical position measured downward from the top of the plate (Supplementary Fig. 3). The maximum fibre stresses occur at $x = x_m$, where the stresses are tensile in the upper half ($z < T_e/2$) and compressive in the lower half ($z > T_e/2$) of the deflected elastic plate.

This distance, x_m, varies as a function of the elastic properties of the shell and is a 3/4-power function of T_e and a 1/4-power function of E (Supplementary Fig. 4). Assuming uniform properties across the ice shell, tensile failure will occur at this distance and parallel to the first fracture. Given $E = 9$ GPa, we find that the maximum stresses occur at a distance of 35 km from the fracture when $T_e \approx 5.2$ km (Supplementary Figs. 3 and 4). Assuming a predominantly conductive ice shell, and taking the elastic layer to correspond to the uppermost part of the ice shell where the temperature is <160 K, this elastic thickness implies a total shell thickness (elastic plus ductile layers) of ~8.9 km, consistent with the polar ice-shell thickness inferred from shape, gravity and libration observations[7]. Whereas ~5.2 km may have been the relevant effective elastic thickness at the time of tiger-stripe formation, subsequent heating or reworking and faulting of the ice shell may have reduced the modern effective elastic thickness to perhaps <2 km, in line with the low end of estimates based on studies of local flexural and tectonic features[38,39]—though we emphasize that these studies provide only a lower bound over the history of Enceladus.

The elastic properties similarly determine how the magnitude of the fibre stresses is related to the magnitude of the load. Given that the maximum tensile stress occurs at $x = x_m$ and $z = 0$, from equation (16), its magnitude is

$$\sigma_{max} = \frac{6M(x_m)}{T_e^2} \tag{17}$$

which can also be written in terms of V_0 as

$$\sigma_{max} = V_0 \frac{6}{T_e^2}\alpha\ \mathrm{e}^{-\pi/4} \sin\frac{\pi}{4} \tag{18}$$

Tensile failure occurs when the load is sufficient to make the bending moment at $x = x_m$ equal to the critical value of

$$M_{crit} = \frac{\sigma_{crit} T_e^2}{6} \tag{19}$$

where σ_{crit} is the tensile failure limit for cold ice, which we take to be 1 MPa for intact ice[40] or 100 kPa for previously weakened ice.

Ice-shell thinning. Here, we assess the possible effect of loss of buoyancy due to thinning ice in the vicinity of an open fissure. We calculate the steady-state temperature distribution around a fissure using a radial-basis-function finite-difference approach. We use an isothermal surface boundary condition of $T_s = 75$ K, and an isothermal boundary condition of $T_m = 273$ K on the crack wall and along the ice–ocean interface (Supplementary Fig. 5a). For the portion of the crack that extends above the level of neutral buoyancy, the temperature varies linearly between the surface temperature and T_m at the upper surface of the water. We applied a far-field insulating boundary condition at a distance of 30 km from the crack. We determine the temperature-dependent thermal conductivity using $k = c/T$, where $c = 651$ W m^{-1} is an experimentally derived constant[41]. For a vertical crack in an ice shell with thickness 12 km, the steady-state conductive heat flow is ~750 W m^{-1} per side.

Once open, the tendency for the fissure to narrow due to freezing is opposed by dissipation as water is cyclically flushed in and out of the fissure[4]. Since the temperature gradient, and therefore the rate of conductive heat loss away from the fissure, is greatest near the surface and decreases towards the base of the fissure, the freezing will be most rapid at the top of the fissure and slower toward its base. We idealize the crack as a wedge shape and estimate the dissipation within the crack as well as the heat conducted away from the crack.

We estimate the steady-state opening angle, θ, for the melt-back wedge illustrated in Supplementary Fig. 5a. Assuming that the crack opens and closes periodically[42], we can write the width of the crack, b, as a function of depth, z, and time, t, as

$$b(z,t) = b_0 + 2z\tan\theta + A\sin(\omega t) \tag{20}$$

where b_0 is the mean width of the crack at the surface, A is the amplitude of the oscillations and ω is the angular frequency. Conservation of mass requires that the velocity of the liquid in the crack, u, be related to the variations in crack width

$$\frac{\partial(ub)}{\partial z} = \frac{\partial b}{\partial t} \tag{21}$$

The energy dissipated by oscillatory flow in a fracture is found by relating the resolved shear stress on the wall, τ, to the mean flow velocity, $\langle u \rangle$, calculated from equation (21), using the Darcy–Weisbach equation

$$\tau = f\frac{1}{2}\rho\langle u\rangle^2 \tag{22}$$

where f is a friction factor and ρ is the fluid density. Because the eruption-driven net outward flow of water is many orders of magnitude slower than the peak velocities in the oscillatory flow, it does not contribute meaningfully to the dissipation and is therefore neglected here. While highly turbulent, the average properties of the flow are in quasi-steady state, and the net acceleration of the water is negligible. The wall shear stress is thus balanced by a dynamic pressure loss per unit depth as

$$2\tau = b\frac{\mathrm{d}P}{\mathrm{d}z} \tag{23}$$

In turn, the rate of energy dissipation per unit volume (Q_v) is related to the rate of decrease in dynamic pressure

$$Q_v = \langle u\rangle\frac{\mathrm{d}P}{\mathrm{d}z} \tag{24}$$

We multiply Q_v by the crack width to obtain the energy dissipated per unit area of crack wall

$$q_d = f\rho\langle u\rangle^3 \tag{25}$$

Dissipation decreases very rapidly with increasing crack width (increasing opening angle). In Supplementary Fig. 5b, we show predicted values of the dissipation

integrated along the wall of the crack for a crack with a surface width of 1 m and an oscillation amplitude of 0.9 m, assuming a friction factor $f = 0.01$ (representative of fully developed turbulent flow in a smooth channel). Owing to the large uncertainties in the crack width, amplitude of oscillation, and friction factor, the dissipation is also very uncertain, but our result nevertheless demonstrates that, if the crack begins to freeze shut, dissipation in the crack becomes much larger than the conducted heat flow, causing melting. On the other hand, dissipation alone cannot produce enough melt-back to achieve opening angles larger than a few hundredths of a degree. Thus, the dissipation mechanism, while capable of preventing the fissure from freezing out[4], does not produce a melt-back wedge wide enough to contribute significantly to the bending stresses discussed above.

Ridge accumulation. Erupted material can accumulate in ridges at the surface, loading the edge of the broken elastic plate from the top. Such a load, per unit length along the fracture, is

$$V_0 = \frac{mg}{L} \tag{26}$$

where m is the mass of accumulated material and L is the total length of the ridges. Given an accumulation rate of $\dot{m}$, the load as a function of time is given by

$$V_0(t) = \frac{\dot{m}g}{L}t \tag{27}$$

The accumulated load gives rise to tensile stresses which are maximum at $x = x_m$ and given by equation (18). Supplementary Fig. 6 shows this maximum tensile stress as a function of time and accumulation rate, with contours indicating two examples of tensile-failure limits. Assuming a tensile-failure limit of 1 MPa and the same elastic properties used in Supplementary Fig. 3, failure occurs when $V_0 = \sim 3.1 \times 10^8\,\mathrm{N\,m^{-1}}$. Assuming an accumulation rate of $10\,\mathrm{kg\,s^{-1}}$ per 100 km length of ridge, the accumulated load would be sufficient to initiate tensile failure after ~875 kyr. As a point of reference, the current total rate of erupted solids has been estimated at $[51 \pm 18]\,\mathrm{kg\,s^{-1}}$, of which 9% is estimated to escape from Enceladus while the remaining 91% falls ballistically back to the surface[25]. The rate of material accumulation per ridge is of course somewhat smaller and depends on how the erupted material is distributed among the tiger stripes, whose rates of activity vary. The eruption rates also vary with time over various timescales[43,44].

The accumulated load may be related to the cross-sectional area, A, of the ridge by

$$V_0 = A\rho_r g \tag{28}$$

where ρ_r is the assumed density of the ridge. Assuming $\rho_r = 900\,\mathrm{kg\,m^{-3}}$, for example, we obtain a load sufficient to generate tensile stresses of 1 MPa when the cross-sectional area of the ridge is $\sim 3\,\mathrm{km}^2$. If the effective tensile failure limit at the time of the tiger stripes' formation is only 100 kPa, then the required ridge cross section is just $\sim 0.3\,\mathrm{km}^2$. Estimating the height ($\lesssim$150 m) and width ($\lesssim$2 km per side) of the present-day ridges from Cassini imagery[12,27] and accounting for the deflection (~120 m) discussed above, the ridge cross-sections may only be $0.2–0.3\,\mathrm{km}^2$ at present. This suggests that our proposed mechanism requires either that the bending-induced failures occurred only after the effective tensile failure limit was reduced to ~100 kPa (perhaps due to pervasive weakening following the formation of the first fissure), or that the ridges were initially larger and have experienced some erosion or relaxation (perhaps due to localized heating) since their formation.

Subsequent fractures. Once the bending stresses are great enough to cause tensile failure at the surface, a new fracture is initiated (Fig. 1b). Whether or not the new fracture can penetrate the ice shell depends on how the stress field evolves during crack propagation. Although this is a dynamic process, we can gain some insight by considering the hypothetical static scenario in which the crack is arrested after propagating a distance y from the surface. At this point, the load, which has not changed on the timescale of crack propagation, would now have to be supported by the partially fractured plate. That is, focusing on the location of the fracture, where $x = x_m$, the bending moment that must be supported remains fixed at M_{crit}, given by equation (19). The fibre stresses in the remaining unbroken part of the lithosphere would have to support the same bending moment but with a reduced effective elastic-layer thickness. The bending stress at the crack tip is thus

$$\sigma_{tip,bending}(y) = \frac{6M_{crit}}{(T_e - y)^2} = \frac{\sigma_{crit}T_e^2}{(T_e - y)^2} \tag{29}$$

where T_e is the initial elastic-layer thickness such that the effective remaining elastic thickness is always $T_e - y$. The bending stresses at the crack tip are therefore always tensile and increasing in magnitude as the crack tip propagates downward through the ice shell (dashed red lines in Supplementary Fig. 7).

This effect is opposed by the background compressive stresses that exist due to overburden pressure, which increases linearly with depth (dotted blue lines in Supplementary Fig. 7), such that the net stress at the crack tip is

$$\sigma_{tip}(y) = \frac{\sigma_{crit}T_e^2}{(T_e - y)^2} - \rho_{ice}gy \tag{30}$$

The gradient as a function of depth is then given by

$$\frac{\mathrm{d}}{\mathrm{d}y}\sigma_{tip}(y) = \frac{2\sigma_{crit}T_e^2}{(T_e - y)^3} - \rho_{ice}g \tag{31}$$

such that $\sigma_{tip}(y)$ increases monotonically with y as long as

$$T_e g < \frac{2\sigma_{crit}}{\rho_{ice}} \tag{32}$$

Provided that equation (32) is satisfied, the tensile stresses due to bending always exceed the compressive stresses due to overburden pressure, such that the net stresses at the crack tip are always tensile, and increasingly so as the crack penetrates deeper through the lithosphere (Supplementary Fig. 7). Hence, once initiated in this way, crack propagation cannot be arrested at any point within the lithosphere. Whereas the condition described by equation (32) is readily satisfied for Enceladus due to its thin ice shell and small gravity, it may not be satisfied for larger bodies or when a thicker elastic layer is present. For example, this condition is not satisfied for Europa unless the elastic-layer thickness is at the low end of the estimated range[29]—less than about 1.5 km (Fig. 2). For Ganymede, Callisto and Titan, the gravity is so strong that the compressive stresses overwhelm the bending stresses for plausible shell thicknesses[29,45–48], precluding rapid crack propagation. Hence, because this situation is permitted only for bodies with low surface gravity, or when the ice shell is extremely thin, Enceladus may be unique among ocean worlds for its ability to develop through-going fractures due to bending stresses (positive or green region of Fig. 2).

What happens when the crack tip reaches the ductile part of the ice? The lower part of the ice shell is ductile on long timescales, and therefore does not participate in the gradually accumulated bending stresses that support the edge loading. If the new fracture is propagating sufficiently rapidly, however, the entire ice shell behaves elastically (the Maxwell time is at least a few hours, even for the low-viscosity ice near the base of the ice shell). That is, as the fracture propagates downward, stresses may build within the otherwise ductile regions of the ice shell, helping to support the load, at least transiently. Determining how this changes the evolution of the stress profile during crack propagation will be the subject of future work.

Data availability

All required data are available in the published literature as indicated.

Code availability

The computer code required to carry out the calculations discussed herein is available on request from the corresponding author.

Received: 8 June 2019; Accepted: 29 October 2019;
Published online: 09 December 2019

References

1. Porco, C. C. et al. Cassini observes the active south pole of Enceladus. *Science* **311**, 1393–1401 (2006).
2. Porco, C., DiNino, D. & Nimmo, F. How the geysers, tidal stresses, and thermal emission across the south polar terrain of Enceladus are related. *Astron. J.* **148**, 45 (2014).
3. Ingersoll, A. P. & Nakajima, M. Controlled boiling on Enceladus. 2. Model of the liquid-filled cracks. *Icarus* **272**, 319–326 (2016).
4. Kite, E. S. & Rubin, A. M. Sustained eruptions on Enceladus explained by turbulent dissipation in tiger stripes. *Proc. Natl Acad. Sci. USA* **113**, 3972–3975 (2016).
5. Manga, M. & Wang, C. Y. Pressurized oceans and the eruption of liquid water on Europa and Enceladus. *Geophys. Res. Lett.* **34**, 1–5 (2007).
6. Rudolph, M. L. & Manga, M. Fracture penetration in planetary ice shells. *Icarus* **199**, 536–541 (2009).
7. Hemingway, D. J. & Mittal, T. Enceladus's ice shell structure as a window on internal heat production. *Icarus* **332**, 111–131 (2019).
8. Postberg, F., Schmidt, J., Hillier, J., Kempf, S. & Srama, R. A salt-water reservoir as the source of a compositionally stratified plume on Enceladus. *Nature* **474**, 620–622 (2011).
9. Iess, L. et al. The gravity field and interior structure of Enceladus. *Science* **344**, 78–80 (2014).

10. Thomas, P. et al. Enceladus's measured physical libration requires a global subsurface ocean. *Icarus* **264**, 37–47 (2016).
11. Spencer, R. et al. in *Enceladus and the Icy Moons of Saturn* (eds Schenk, P. M., Clark, R. N., Howett, C. J. A. & Verbiscer, A. J.) 163–174 (Univ. Arizona Press, 2018).
12. Patthoff, D. A. & Kattenhorn, S. A. A fracture history on Enceladus provides evidence for a global ocean. *Geophys. Res. Lett.* **38**, 1–6 (2011).
13. Bland, M. T., McKinnon, W. B. & Schenk, P. M. Constraining the heat flux between Enceladus' tiger stripes: numerical modeling of funiscular plains formation. *Icarus* **260**, 232–245 (2015).
14. Yin, A. & Pappalardo, R. T. Gravitational spreading, bookshelf faulting, and tectonic evolution of the south polar terrain of Saturn's moon Enceladus. *Icarus* **260**, 409–439 (2015).
15. Yin, A., Zuza, A. V. & Pappalardo, R. T. Mechanics of evenly spaced strike-slip faults and its implications for the formation of tiger-stripe fractures on Saturn's moon Enceladus. *Icarus* **266**, 204–216 (2016).
16. Nakajima, M. & Ingersoll, A. P. Controlled boiling on Enceladus. 1. Model of the vapor-driven jets. *Icarus* **272**, 309–318 (2016).
17. Nimmo, F., Barr, A. C., Běhounková, M. & Mckinnon, W. B. in *Enceladus and the Icy Moons of Saturn* (eds Schenk, P. M., Clark, R. N., Howett, C. J. A. & Verbiscer, A. J.) 79–94 (Univ. Arizona Press, 2018).
18. Kamata, S. & Nimmo, F. Interior thermal state of Enceladus inferred from the viscoelastic state of the ice shell. *Icarus* **284**, 387–393 (2017).
19. Čadek, O., Běhounková, M., Tobie, G. & Choblet, G. Viscoelastic relaxation of Enceladus's ice shell. *Icarus* **291**, 31–35 (2017).
20. Choblet, G. et al. Powering prolonged hydrothermal activity inside Enceladus. *Nat. Astron.* **1**, 841–487 (2017).
21. Tajeddine, R. et al. True polar wander of Enceladus from topographic data. *Icarus* **295**, 46–60 (2017).
22. Nimmo, F. & Pappalardo, R. T. Diapir-induced reorientation of Saturn's moon Enceladus. *Nature* **441**, 614–6 (2006).
23. Roberts, J. H. & Stickle, A. M. Break the world's shell: an impact on Enceladus: bringing the ocean to the surface. In *Lunar and Planetary Science* XLVIII 1955 (LPI, 2017).
24. Nimmo, F., Spencer, J. R., Pappalardo, R. T. & Mullen, M. E. Shear heating as the origin of the plumes and heat flux on Enceladus. *Nature* **447**, 289–91 (2007).
25. Ingersoll, A. P. & Ewald, S. P. Total particulate mass in Enceladus plumes and mass of Saturn's E ring inferred from Cassini ISS images. *Icarus* **216**, 492–506 (2011).
26. Degruyter, W. & Manga, M. Cryoclastic origin of particles on the surface of Enceladus. *Geophys. Res. Lett.* **38**, L16201 (2011).
27. Crow-Willard, E. N. & Pappalardo, R. T. Structural mapping of Enceladus and implications for formation of tectonized regions. *J. Geophys. Res. Planets* **120**, 928–950 (2015).
28. Turcotte, D. L. & Schubert, G. *Geodynamics* (Cambridge Univ. Press, 1982).
29. Billings, S. E. & Kattenhorn, S. A. The great thickness debate: ice shell thickness models for Europa and comparisons with estimates based on flexure at ridges. *Icarus* **177**, 397–412 (2005).
30. tenBrink, U. Volcano spacing and plate rigidity. *Geology* **19**, 397–400 (1991).
31. Hieronymus, C. F. & Bercovici, D. Discrete alternating hotspot islands formed by interaction of magma transport and lithospheric flexure. *Nature* **397**, 604–607 (1999).
32. Nimmo, F. Non-Newtonian topographic relaxation on Europa. *Icarus* **168**, 205–208 (2004).
33. Nimmo, F., Pappalardo, R. T. & Giese, B. Effective elastic thickness and heat flux estimates on Ganymede. *Geophys. Res. Lett.* **29**, 1158 (2002).
34. Kalousová, K., Soucek, O. & Cadek, O. Deformation of an elastic shell with variable thickness: a comparison of different methods. *Geophys. J. Int.* **190**, 726–744 (2012).
35. Crouch, S. L. & Starfield, A. M. *Boundary Element Methods in Solid Mechanics* (George Allen and Unwin, 1983).
36. Qin, R., Buck, W. R. & Germanovich, L. Comment on "Mechanics of tidally driven fractures in Europa's ice shell" by S. Lee, R. T. Pappalardo, and N. C. Makris [2005. *Icarus* **177**, 367–379]. *Icarus* **189**, 595–597 (2007).
37. Dombard, A. J., Patterson, G. W., Lederer, A. P. & Prockter, L. M. Flanking fractures and the formation of double ridges on Europa. *Icarus* **223**, 74–81 (2013).
38. Bland, M. T., Beyer, R. A. & Showman, A. P. Unstable extension of Enceladus' lithosphere. *Icarus* **192**, 92–105 (2007).
39. Giese, B. et al. Enceladus: an estimate of heat flux and lithospheric thickness from flexurally supported topography. *Geophys. Res. Lett.* **35**, 1–5 (2008).
40. Hammond, N. P., Barr, A. C., Cooper, R. F., Caswell, T. E. & Hirth, G. Experimental constraints on the fatigue of icy satellite lithospheres by tidal forces. *J. Geophys. Res. Planets* **123**, 1–15 (2018).
41. Petrenko, V. F. & Whitworth, R. W. *Physics of Ice* (Oxford Univ. Press, 1999).
42. Hurford, T. A., Helfenstein, P., Hoppa, G. V., Greenberg, R. & Bills, B. G. Eruptions arising from tidally controlled periodic openings of rifts on Enceladus. *Nature* **447**, 292–294 (2007).
43. Nimmo, F., Porco, C. & Mitchell, C. Tidally modulated eruptions on Enceladus: Cassini ISS observations and models. *Astron. J.* **148**, 46 (2014).
44. Ingersoll, A. P. & Ewald, S. P. Decadal timescale variability of the Enceladus plumes inferred from Cassini images. *Icarus* **282**, 260–275 (2017).
45. Spohn, T. & Schubert, G. Oceans in the icy Galilean satellites of Jupiter? *Icarus* **161**, 456–467 (2003).
46. Béghin, C., Sotin, C. & Hamelin, M. Titan's native ocean revealed beneath some 45 km of ice by a Schumann-like resonance. *C. R. Geosci.* **342**, 425–433 (2010).
47. Hemingway, D. J., Nimmo, F., Zebker, H. & Iess, L. A rigid and weathered ice shell on Titan. *Nature* **500**, 550–552 (2013).
48. Vance, S., Bouffard, M., Choukroun, M. & Sotin, C. Ganymede's internal structure including thermodynamics of magnesium sulfate oceans in contact with ice. *Planet. Space Sci.* **96**, 62–70 (2014).

Acknowledgements

This work was made possible by the NASA/ESA Cassini mission to Saturn and, in particular, the work of the Imaging Science Subsystem team. D.J.H. was funded in part by the Miller Institute for Basic Research in Science at the University of California Berkeley and in part by the Carnegie Institution for Science in Washington DC. D.J.H. and M.M. acknowledge support from the Center for Integrative Planetary Science (CIPS) at the University of California Berkeley. M.M. was supported in part by NASA Solar System Workings grant 80NSSC19K0557. M.L.R. was supported in part by NSF DMS-1624776. We thank the CIDER working group, supported by NSF EAR-1135452, for early discussions that contributed to parts of this work. We thank M. Bland, R. Citron, J. Jordan, S. Kattenhorn, E. Kite and T. Mittal for helpful discussions.

Author contributions

M.M. developed the analytical equations for the secular cooling-induced tangential stresses in the ice shell. M.L.R. developed the analytical and boundary element models for crack penetration for the first fracture and carried out the related calculations. M.L.R. computed the relationship between turbulent dissipation in the fissure and the crack opening angle. D.J.H. proposed the mechanism of forming subsequent parallel fractures due to bending stresses and carried out the related calculations. D.J.H. drafted the manuscript with input from M.M. and M.L.R. All authors discussed the analysis and reviewed and commented on the manuscript.

Competing interests

The authors declare no competing interests.

Additional information

Supplementary information is available for this paper at https://doi.org/10.1038/s41550-019-0958-x.

Correspondence and requests for materials should be addressed to D.J.H.

Peer review information *Nature Astronomy* thanks Gaël Choblet and An Yin for their contribution to the peer review of this work.

Reprints and permissions information is available at www.nature.com/reprints.

Publisher's note Springer Nature remains neutral with regard to jurisdictional claims in published maps and institutional affiliations.